

**Impact of impurities on drift wave instabilities in reversed-field pinch plasmas**Jingchun Li <sup>\*</sup>*Department of Earth and Space Sciences, Southern University of Science and Technology,  
518055 Shenzhen, Guangdong, People's Republic of China*Songfen Liu<sup>†</sup> and Yilong Zhang*School of Physics, Nankai University, Tianjin 300071, People's Republic of China*

Jiaqi Dong

*ENN Science and Technology Development Co., Ltd., Langfang 065001, China*

Wei Kong

*College of Science, Civil Aviation University of China, Tianjin 300300, People's Republic of China*

P. Shi

*United Kingdom Atomic Energy Authority, Culham Centre for Fusion Energy, Culham Science Centre,  
Abingdon, Oxon OX14 3DB, United Kingdom*

(Received 8 March 2022; revised 15 September 2022; accepted 22 September 2022; published 12 October 2022)

The drift wave in the presence of impurity ions was investigated numerically in reversed-field pinch plasmas, using the gyrokinetic integral eigenmode equation. By comparing the results of regular and hollow plasma density profiles, it was found that the ion temperature gradient mode for the hollow density profile case is much harder to excite. For the impurity effects, when the impurity density gradient is opposite to the electrons, namely when  $L_{ez}$  ( $L_{ez} = L_{ne}/L_{nz}$  with  $1/L_n$  being the density gradient scale length, and the subscript “e” and “z” indicates electrons and impurity ions, respectively) is negative, the impurities can enhance the instability. On the contrary, when  $L_{ez}$  is positive, the instability is stabilized. Regarding the trapped electron mode (TEM), the growth rate for plasmas with a hollow density profile remains smaller than that of the standard density gradient. There exists a threshold in  $L_{ez}$ . When  $L_{ez}$  is less than this value, the impurities destabilize the TEMs, while when  $L_{ez}$  is greater than this value, the impurities stabilize the TEMs. In addition, the influence of the collisionality on the TEMs was also studied.

DOI: [10.1103/PhysRevE.106.045203](https://doi.org/10.1103/PhysRevE.106.045203)**I. INTRODUCTION**

In the toroidal plasma microscopic instability occurs when the plasma deviates from the state of thermodynamic equilibrium. As the plasma develops into a nonlinear saturation state, plasma turbulence will be generated, which causes macroscopic turbulent transport [1–5]. Among these perturbations, ion temperature gradient (ITG) instability has been proven to be the primary contribution causing anomalous transport in the core of tokamak plasmas with theory and experiment [6–8]. As one kind of electron drift waves, the trapped electron mode (TEM) is driven by a trapped electron pressure gradient, and offers an important effect on electron anomalous transport. Whether microscopic instabilities such as ITG and TEM also play important roles in the transport in reversed-field pinches (RFPs), is an even more open issue. In fact the study of microturbulence has already been extended to

the RFP configuration [9]. Previous studies have shown that ITG instabilities can be considered as a partial contributor to particle/energy transport in the RFP [10]. Nevertheless, more careful analysis of the ITG and TEM stability should be performed because higher performances have been obtained in RFP plasmas, and one should consider the role possibly played by the drift wave turbulence for further improving the confinement in RFP plasmas. Moreover, in the actual operation of a toroidal plasma, particle injection often leads to an abnormal (hollow) distribution of the plasma density [11,12], and the generation of impurities is also unavoidable [13,14]. Therefore, understanding impurities and their influence on the microturbulence in RFP plasmas with both normal and hollow density profiles is one of the critical challenges that magnetically confined fusion plasmas face [15,16].

In the RFX-mod, the axisymmetric and helical RFP configuration with different  $q(a)$  states (reduced from 4 to 1.2) have been studied experimentally [17]. In this device two transmission parameters, namely the diffusion coefficient and the convection velocity, have been determined, and previous works also confirmed the presence of external velocity bar-

<sup>\*</sup>jingchunli@pku.edu.cn;lijc@sustech.edu.cn<sup>†</sup>lsfnku@nankai.edu.cn

riers for light impurities [18]. In terms of particle injection [19–21], experiments in RFP plasmas have also been carried out in the Madison Symmetric Torus RFP [22]. Therefore, instability analysis under RFP hollow plasmas thus becomes significant.

The microinstability related to the hollow density profile in a toroidal plasma has been theoretically investigated in recent years [23,24]. Under the slab configuration with magnetic shear, the instability driven by the electron temperature gradient in a plasma with a slight hollow density profile was studied using the gyrokinetic integral eigenvalue equation, showing the suppression effect of shear flow in transport [25]. Using the eigenmode equation, the ITG mode was modeled numerically in the presence of impurity ions and trapped electrons (TEs) in the tokamak plasma with a hollow density distribution. It was found that, in the hollow density plasma, the increase of ion temperature gradient results in an increase of the ITG growth rate and frequency, and that the density gradient plays an important role in the ITG mode [26].

For the RFP configurations, when considering impurities, the RFX-mod device usually exhibits a hollow carbon/oxygen distribution, which peaks in the edge region. Reference [27] calculated the ITG instability and gyrokinetic results of turbulence, and described the role of impurities in the ITG mode instability. Reference [28] used a gyrokinetic integral equation containing trapped electrons and impurity ions to study the electrostatic mode driven by ITG in RFP plasma. It was proved that, when the density gradient is opposite to the primary ion, the impurity ions cause an increase in the ITG instability, and the TEs also have a destabilizing effect on the ITG mode. Reference [29] studied the stability threshold of the ITG mode through the linear gyrokinetic theory, showing that the temperature slope required to excite the ITG instability is much steeper than that of tokamak. In addition, Refs. [30,31] considered TEs and all-ion kinetic effects, and found that the role of TEs becomes important in RFP only under a very steep density/temperature gradient. Compared with the tokamak plasma, the instability of TEM in the RFP plasma requires a much larger density/temperature gradient, and the  $k_\theta \rho_s$  spectrum is much narrower.

To summarize, the impurities and their influence on micro-turbulence in tokamaks have been clarified. However, these effects have not been investigated in RFP plasmas; in particular, the impurity effect on the TEMs remains unclear. Besides, the characteristics of ITG and TEM instability in RFPs with a hollow density have never been reported. In this work, the drift wave instability is studied under RFP configurations. We considered both collisionless and collisional RFP plasmas with standard and hollow density profiles. By comparing the results of the typical plasma density profile ( $\varepsilon_n > 0$ , where  $\varepsilon_n = L_{ne}/R$  is the inverse of the density gradient with  $R$  being the major radius) and the hollow plasma density profile ( $\varepsilon_n < 0$ ), it is shown that the growth rate of the ITG instability in the plasma with the recessed density profile is lower and is harder to excite. Moreover, when  $L_{ez}(L_{ez} = L_{ne}/L_{nz}$ ,  $L_n = -(d \ln(n)/dr)^{-1}$  is the inverse of the density gradient scale length, and the subscripts “e”, “z”, and “i” indicate electrons, impurity ions, and ions, respectively) are positive, the impurities can stabilize the instability, while when  $L_{ez}$  is negative, the impurities enhance the instability. Regarding the

TEMs, the growth rate for the plasma with a hollow density profile remains smaller than that for the plasma with a standard density profile. Moreover, the collisionality can stabilize the TEMs.

The remainder of this article is organized as follows. The HD7 code and the numerical results are introduced in Sec. II. The results of ITG instability in RFPs are presented in Sec. II A. The simulation of TEM is analyzed in Sec. II B. Finally, the conclusions are drawn in Sec. III.

## II. SIMULATION RESULTS

In the RFP configuration, the toroidal magnetic field reverses in the edge of plasma during the plasmas relaxation, and has the same order of magnitude as that of the poloidal magnetic field. As a consequence, the poloidal magnetic field has to be incorporated into the total magnetic field. This is the main difference between tokamak and RFP plasmas. Hence the toroidal and poloidal magnetic fields in RFPs are presented by  $B_\phi = B_{\phi 0}(1 - \epsilon \rho \cos \theta)$  and  $B_\theta = B_{\theta 0}(1 - \Lambda \cos \theta)$ , respectively. Here,  $B_{\phi 0}$  and  $B_{\theta 0}$  are the equilibrium toroidal and poloidal magnetic fields at the magnetic axis, respectively,  $\epsilon = a/R_0$  ( $R_0$  is the major radius) is the inverse aspect-ratio,  $\rho = r/a$  is the normalized minor radius,  $\theta$  is the poloidal angle, and  $\Lambda$  expresses the poloidal variation of  $B_\theta$ . The parameter  $\Lambda = \Lambda(\epsilon, B_{\theta 0})$  changes with the poloidal magnetic field  $B_{\theta 0}$ . More detailed discussions on this concern may be found in Refs. [29–32].

In this section, we use the integral eigenvalue code HD7 to study the micro-instabilities in RFP configurations. The integral eigenvalue equation can be found in Ref. [28] and is neglected here. The term of the density perturbation of TEs is previously reported in Ref. [30] [namely Eq. (4) therein], and we will give a derivation of this formula in detail in the Appendix. The HD7 code has been modified by applying it to RFP configurations [28,30,31,33] and updated in this work. Under the RFP configuration, the results calculated by HD7 are similar to those obtained by codes such as GS2 [34] and TRB [35]. In the calculation, the mode frequency is normalized to electron diamagnetic drift frequency  $\omega_{*e} = ck_\theta T_e / eBL_{ne}$ , and the wave numbers are normalized to  $\rho_s^{-1} = eB/c\sqrt{2T_e m_i}$ , where  $c$  is the speed of light,  $k$  the wave number,  $B$  the total magnetic field strength,  $e$  the electric charge of electron,  $m_i$  the mass of the ions, and  $T_e$  the temperature of electrons.

We have conducted one benchmark case of the results provided by HD7 with the gyrokinetic codes GENE [36] with the following parameters:  $r/R_0 = 0.068$ , the safety factor  $q = 0.15$ , the magnetic shear  $\hat{s} = 0.3$ ,  $R/L_n = 5.89$ ,  $R/L_{Ti} = R/L_{Te} = 4.45$ ,  $n_e = 5.88 \times 10^{13} \text{ cm}^{-3}$ ,  $T_i = 0.99 \text{ KeV}$ ,  $T_e = 1.29 \text{ KeV}$ . The comparison is presented in Fig. 1. The results show that the two curves almost lie on top of each other, which indicates the HD7 code benchmarked against well with the GENE code.

We first study the ITG mode. The default parameters we utilized were:  $q = 0.15$ ,  $\hat{s} = 1.0$ , the temperature ratio  $\tau_i = T_e/T_i = 1.33$ ,  $\tau_z = T_e/T_z = 1.33$ ,  $\eta_z = L_{ne}/L_{Tz} = 16$ ,  $k_\theta \rho_s = 0.447$ , the trapped electrons concentration  $\varepsilon = 0.0$  unless otherwise stated.

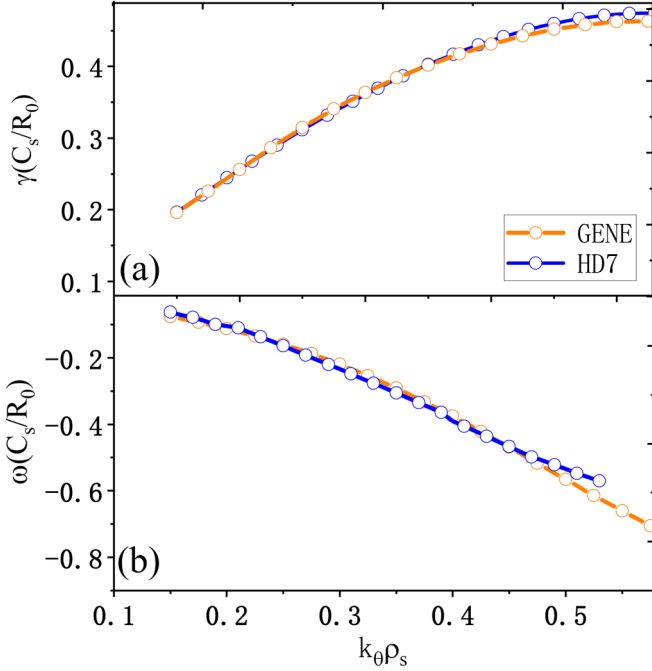


FIG. 1. The comparison of ITG growth rate (a) and real frequency (b) between HD7 and GENE codes.

### A. ITG modes

First, the effects of the ion temperature gradient  $R/L_{Ti}$  and density gradient  $R/L_n$  on the ITG modes are discussed because they are generally believed to provide the driving force for the ITG modes. The normalized growth rates of the pure ITG modes as a function of  $R/L_{Ti}$  and  $R/L_n$  are illustrated in Figs. 2(a) and 2(b), respectively. We can see from Fig. 2(a) that the growth rate of the ITG modes increases with the increase in  $R/L_{Ti}$ . The larger the absolute value of  $R/L_n$  is, the greater the growth rate of the ITG modes is. Figure 2(b) shows that the smaller the  $R/L_{Ti}$ , the smaller the ITG growth rates. At the same time, when the absolute values of  $R/L_n$  are equal, the growth rate corresponding to positive  $R/L_n$  ratios is much larger. This indicates that the ITG mode in plasmas with a hollow density profile will be relatively difficult to excite in both the strong and weak density gradient cases compared with plasmas with typical density profiles. It is also possible to see that the growth rate is always monotonous when keeping the  $R/L_n$  ratio constant. We can conclude that a high  $R/L_{Ti}$  enhances the ITG instability, and it is easier to trigger the ITG mode in RFP plasmas with a standard density profile.

The normalized real frequency and growth rate as a function of the charge concentration  $f_z$  of fully ionized carbon impurities in plasmas with regular and hollow density profiles are represented in Fig. 3. Figures 3(a) and 3(c) show that the ITG frequency and growth rate change monotonically with  $f_z$ . With positive values of  $L_n$ , it is clearly demonstrated that  $L_{ez} = 2$  has a stabilizing effect on the modes, while  $L_{ez} = -6$  has a destabilizing impact on the modes. It is thus possible to conclude that when the impurity ion density gradient is opposite to that of the electrons ( $L_{ez} < 0$ ), the ITG instability is enhanced. On the contrary, when  $L_{ez} > 0$ , the growth rate of the ITG instability is reduced. These findings

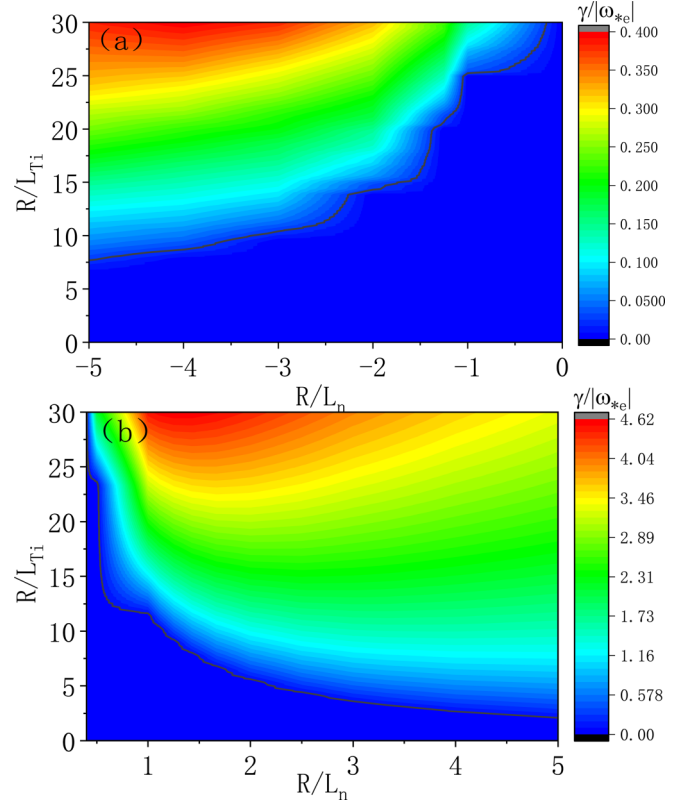


FIG. 2. Contour plots of the normalized real frequency of the ITG mode in the plane of the normalized ion temperature gradient  $R/L_{Ti}$  and density gradients  $R/L_n$  in pure plasma ( $f_z = 0$ ). (a) and (b) correspond to the plasma with a hollow density profile and a normal density profile, respectively. Other parameters are  $\hat{s} = 0.3$ ,  $\tau_i = 1.33$ ,  $k_\theta \rho_s = 0.447$ ,  $\varepsilon = 0.0$ ,  $q = 0.15$ . Below the black line is the stable region.

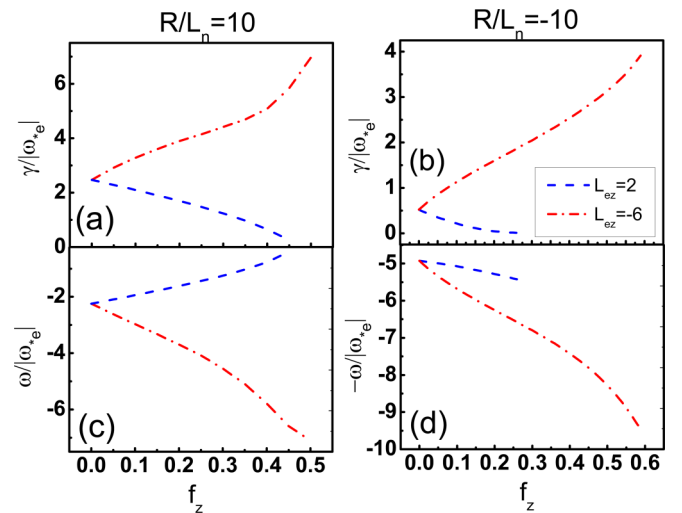


FIG. 3. Normalized real frequency and growth rate versus charge concentration  $f_z$  of the fully ionized carbon impurity in plasmas with normal density profile (a),(c) and hollow density profile (b),(d). Other parameters are  $\hat{s} = 1.0$ ,  $\tau_i = \tau_z = 1.33$ ,  $\eta_z = 16$ ,  $k_\theta \rho_s = 0.447$ ,  $\varepsilon = 0.0$ ,  $q = 0.15$ .

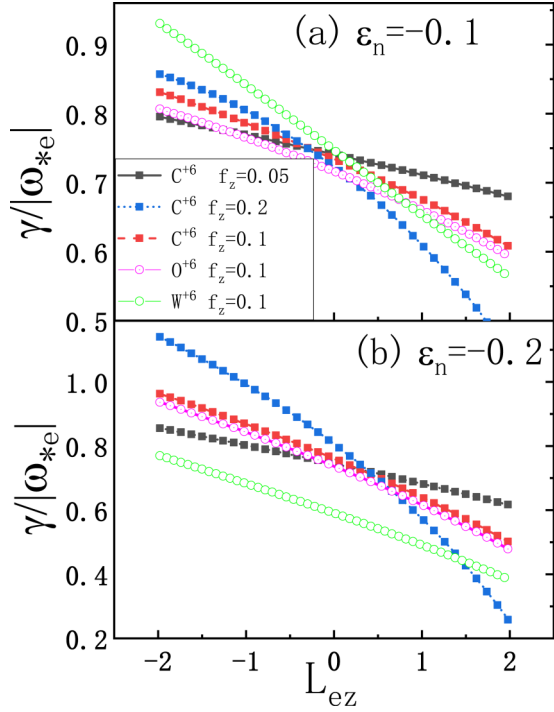


FIG. 4. Normalized real frequency and growth rate versus  $L_{ez}$  for different impurity charge concentrations  $f_z$  as well as different impurity species. The other parameters are  $\hat{s} = 1.0$ ,  $\tau_i = \tau_z = 1.33$ ,  $\eta_i = 0$ ,  $\eta_z = 16$ ,  $k_\theta \rho_s = 0.447$ ,  $\varepsilon = 0.0$ ,  $q = 0.15$ ,  $z = 6$  (carbon).

are consistent with previous simulation results discussed in Refs. [26,28]. Figures 3(b) and 3(d) display the growth rate and real frequency of the ITG modes for the hollow density case. It can be seen that these results are very similar to those for the non-hollow density profile case when  $L_{ez} < 0$ ; the ITG instability is reinforced. On the other hand, when  $L_{ez} > 0$ , the ITG growth rate first increases and then decreases with  $f_z$ . Furthermore, the greater  $|L_{ez}|$ , the greater the stabilizing/destabilizing effects. With a hollow density profile, the small growth rate of the ITG mode can still be seen in Fig. 3(b). Figures 3(a) and 3(c) also reveal that the charge concentration can enhance the stabilizing/destabilizing effects of the carbon impurities.

To further investigate the effect of  $L_{ez}$  on the ITG modes, we scanned  $L_{ez}$  for different density gradients. The normalized growth rate as a function of  $L_{ez}$  is shown in Fig. 4 for different impurity charge concentrations of carbon. It shows that when  $L_{ez}$  is positive, the impurities have a stabilizing effect. The larger the number of impurities, the stronger the stabilizing effect; on the other hand, when  $L_{ez}$  is negative, the presence of impurities has a destabilizing effect. Besides, the influence of  $L_{ez}$  on the ITG instability for plasmas with hollow and non-hollow density profiles is the same. The obvious difference is that in the case of the hollow density profile, the ITG growth rate is lower. Since there are many impurity ions with different ionization states in RFP plasmas, we investigate their impact individually as also shown in Fig. 4. Here, we consider the influence of the  $O^{+6}$ ,  $C^{+8}$ , and  $W^{+8}$  impurities with varying ionization states. It is found that the growth rate of the ITG mode gradually decreases with the increase in

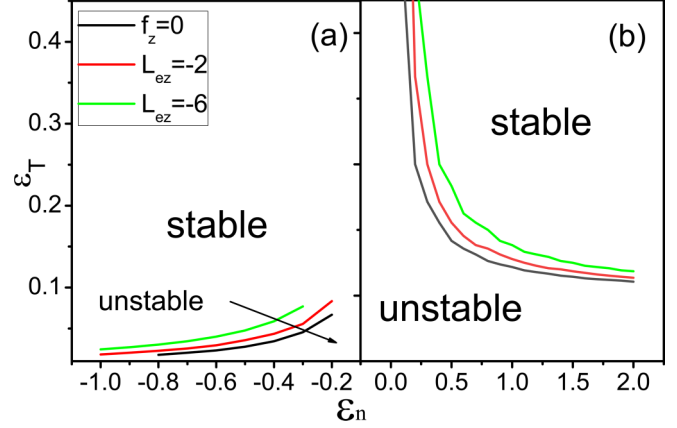


FIG. 5. Thresholds for ITG in the ion temperature gradient ( $\varepsilon_T = L_T/R$ ) and density gradient ( $\varepsilon_n = L_n/R$ ) plane in pure and mixture plasmas with hollow (a) and normal (b) density profiles. Other parameters are  $\hat{s} = 1.0$ ,  $\tau_i = \tau_z = 1.33$ ,  $\eta_i = 0$ ,  $\eta_z = 16$ ,  $k_\theta \rho_s = 0.447$ ,  $\varepsilon = 0.0$ ,  $q = 0.15$ ,  $z = 6$  (carbon).

the impurity mass. Due to the extremely high mass number of tungsten, when  $\varepsilon_n = -0.1$ , this phenomenon is offset to a certain extent. These results suggest that heavy impurities, such as tungsten, have a better stabilizing effect on the ITG mode.

Finally, we investigated the ITG stability threshold considering carbon impurities. Figure 5 displays the temperature gradient threshold  $\varepsilon_T$  for the ITG instability as a function of  $\varepsilon_n$  for different  $L_{ez}$  values for both hollow [Fig. 5(a)] and standard [Fig. 5(b)] density profiles. Figures 5(a) and 5(c) suggest that the threshold decreases with increasing the absolute value of  $\varepsilon_n$ , and the larger  $\varepsilon_n$  is, the more difficult it becomes for the ITG instability to be excited. However, the sign of  $\varepsilon_n$  influences  $\varepsilon_T$ , and the  $\varepsilon_T$  corresponding to the positive  $\varepsilon_n$  is larger than the  $\varepsilon_T$  corresponding to the negative one; that is, the modes with a positive  $\varepsilon_n$  are more unstable. Impurities with a negative  $L_{ez}$  can destabilize the mode and weaken the Landau damping effects of the primary ion in RFP plasmas. Regardless of whether it is a hollow density or a normal density gradient, when impurities exist, and their density gradient is opposite to that of the plasma, the instability interval will increase. Overall, since the excitation range for the hollow density gradient is narrower than for the positive density gradient, the ITG in the hollow plasma is more difficult to trigger. These results are in agreement with cases in tokamaks [26]. In RFP plasmas, when the density is large, the temperature gradient interval of the ITG instability is relatively large. Thus, impurities with a negative  $L_{ez}$  enhance the ITG modes in RFP plasmas. Nevertheless, if the negative  $L_{ez}$  and negative density gradients are sufficiently strong, the stability threshold  $\varepsilon_T$  in hollow density plasmas can reach the order of magnitude of that of normal density RFP plasmas.

## B. TEMs

In this section, we focus on the TEM instabilities in RFP plasmas with a hollow density profile and compare the results with those obtained for normal density profile plasmas. Unless otherwise stated, the parameters we adopted are as follows:

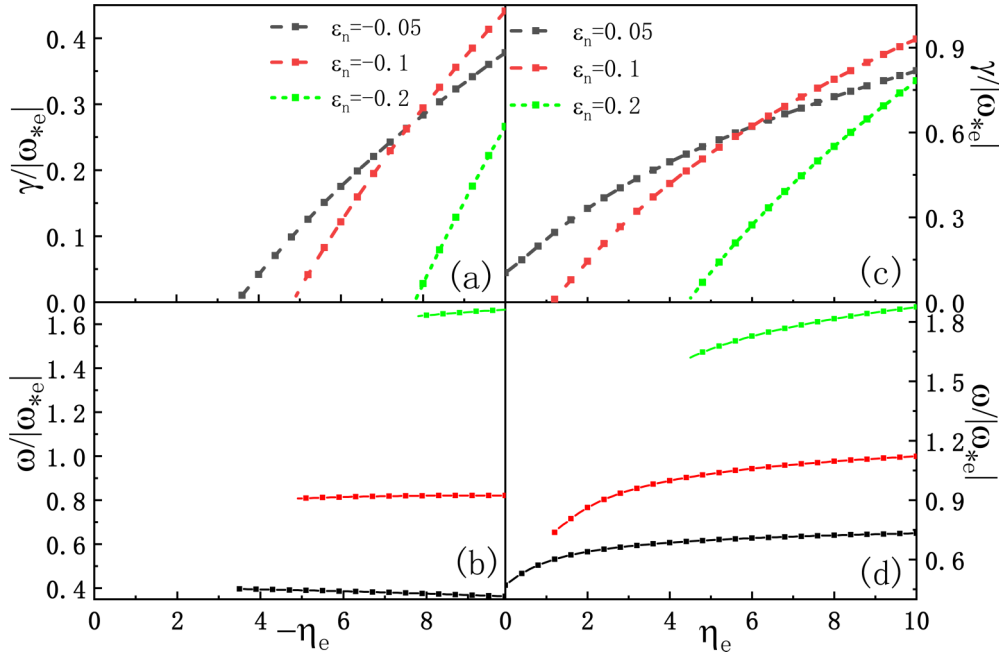


FIG. 6. Normalized growth rate  $\gamma/|\omega_{*e}|$  and real frequency  $\omega/|\omega_{*e}|$  of TEM versus  $\eta_e$  under normal density profile (a),(b) and hollow density profile (c),(d). Other parameters are  $\hat{s} = 0.5$ ,  $\tau_i = 1.33$ ,  $k_\theta \rho_s = 0.447$ ,  $\varepsilon = 0.15$ ,  $q = 0.15$ .

$\hat{s} = 0.5$ ,  $\eta_i = 0$ ,  $\tau_i = 1.33$ ,  $k_\theta \rho_s = 0.447$ ,  $\varepsilon = 0.15$ , and  $q = 0.15$ . These parameters are typical characteristic parameters of the TEM excitation in RFP plasmas.

The TEMs in pure RFP plasmas are discussed first. Figure 6 depicts the normalized growth rate  $\gamma/|\omega_{*e}|$  and real frequency  $\omega/|\omega_{*e}|$  of the TEMs as a function of  $\eta_e$  for the normal density profile (a),(b) and hollow density profile (c),(d) cases. This figure illustrates that  $\eta_e$  provides the driving force for the TEM excitation. For the hollow density case, the TEM growth rate varies with  $\eta_e$ , which is similar to the non-hollow density case. Similar to the ITG mode, the difference between the hollow and non-hollow density profiles lies in the fact that the growth rates of TEM for the hollow density profile plasma are smaller. Indeed, the growth rate is around half of that observed for the non-hollow density profile plasma at the maximum growth rate. These calculations indicate that the TEM instability in RFP plasmas with a hollow density profile requires a very steep density profile compared with the case of plasmas with a non-hollow density profile.

We carried out investigations of the impurity effects on the TEMs. As mentioned earlier, compared with the non-hollow density case, the predominant difference in the TEMs for the hollow density plasma is that their stable interval is smaller, and they are not easy to excite. Here, we mainly concentrate on the impact of impurity ions on the TEMs for the hollow density plasma. Figure 7 depicts the normalized growth rate  $\gamma/|\omega_{*e}|$  and real frequency  $\omega/|\omega_{*e}|$  of TEMs as a function of  $L_{ez}$  for the hollow density profile case; carbon  $C^{+6}$  is taken as the impurity. In the presence of impurities, the relationship between the change in the TEMs and the change in  $L_{ez}$  is similar to that of the ITG with  $L_{ez}$ ; that is, as  $L_{ez}$  increases (from negative to positive), the growth rate of the TEMs decreases. Note that there is a threshold value for  $L_{ez}$ . We refer to it as  $L_{ezt}$ . When  $L_{ez}$  is less than  $L_{ezt}$ , the impurities destabilize the

TEMs, while when  $L_{ez}$  is greater than this value, the impurities stabilize the TEMs. For the three  $f_z$  cases investigated here, the corresponding  $L_{ezt}$  is around  $-1$ .

We then studied the effect of different impurity species. Figure 8 shows the normalized growth rate  $\gamma/|\omega_{*e}|$  and real frequency of the TEMs as a function of  $L_{ez}$  for the hollow density profile case with different impurities (namely,  $C^{+6}$ ,  $O^{+6}$ , and  $W^{+6}$ ,  $W^{+12}$ , and  $W^{+18}$  with  $f_z = 0.1$ ). It can be

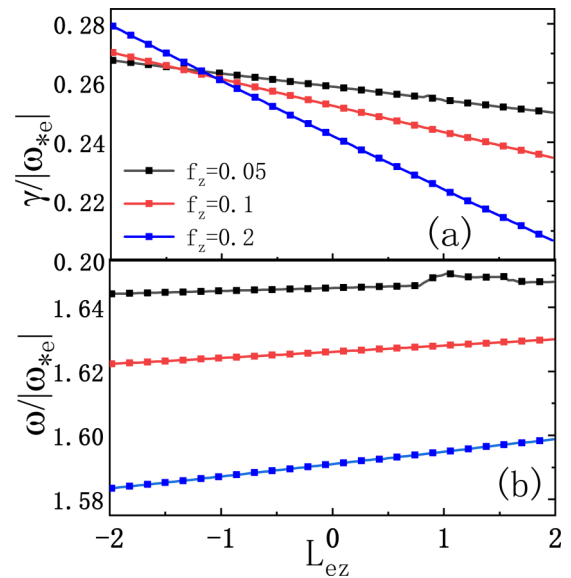


FIG. 7. Normalized growth rate  $\gamma/|\omega_{*e}|$  (a) and real frequency  $\omega/|\omega_{*e}|$  (b) of TEM versus  $L_{ez}$  under hollow density profile with different impurity charge concentration. Other parameters are  $\hat{s} = 0.5$ ,  $\tau_i = \tau_z = 1.33$ ,  $\eta_i = 0$ ,  $\eta_e = 10$ ,  $k_\theta \rho_s = 0.447$ ,  $\varepsilon = 0.15$ ,  $q = 0.15$ ,  $z = 6$  (carbon).

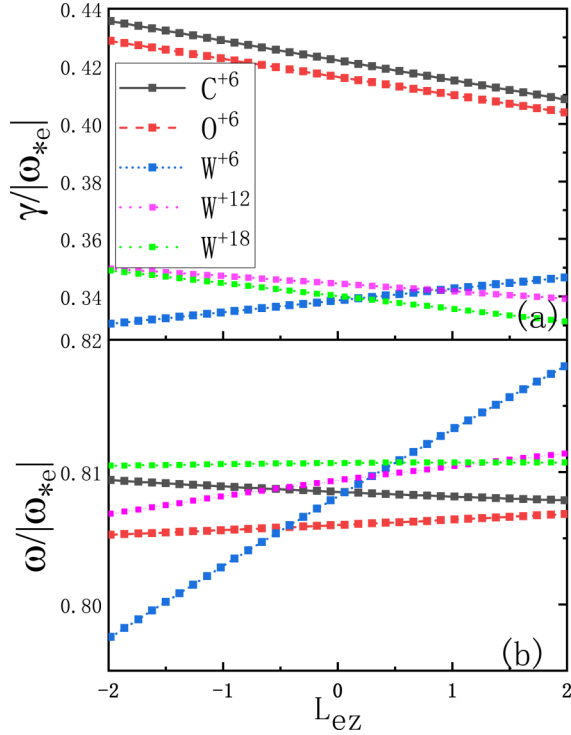


FIG. 8. Normalized growth rate  $\gamma/|\omega_{*e}|$  (a) and real frequency  $\omega/|\omega_{*e}|$  (b) of TEM versus  $L_{ez}$  under hollow density profile with different impurities ( $f_z = 0.1$ ). Other parameters are the same as those used in Fig. 6.

seen that, for the normal density profile case and for the three lighter ions, namely  $C^{+6}$  and  $O^{+8}$ , as  $L_{ez}$  increases, the

TEM growth rate decreases, while the opposite occurs for the heavy-ion  $W^{+6}$ . Besides, there is a mild dependence of the real frequency on  $L_{ez}$  for  $C^{+6}$  and  $O^{+6}$ ; on the other hand, when the  $W^{+6}$  ion is used as the impurity, the real frequency increases with  $L_{ez}$ . In general, both the  $C^{+6}$  and  $O^{+8}$  impurities reduce the growth rate of the TEMs. This is due to the fact that the finite Larmor radius of larger impurity ions can suppress the TEM instability. In addition, similar to the ITG mode, also the heavy tungsten impurity exhibits a particular characteristic. For W impurities with different charge numbers, the growth rate of the TEMs decreases with the increase in  $L_{ez}$ , and for  $W^{+6}$ , the growth rate of the TEMs increases with the increase in  $L_{ez}$ . However, tungsten has a more pronounced stabilizing effect on the TEMs in comparison with that of other light impurities. This difference may be due to the fact that heavier impurity ions have a smaller thermal velocity; thus, the fluid condition ( $\omega \gg k_{||}v_{||}$ ) is easily satisfied, which will weaken the wave-particle resonance effect, leading to more stable TEMs. Therefore, we can say that heavy ions with the same ionization state and different masses can easily suppress the TEM instability. In this sense, tungsten is indeed an ideal first-wall material.

The effect of the collisionality on the trapped electron mode was finally investigated. Fig. 9 depicts the normalized growth rate  $\gamma/|\omega_{*e}|$  and real frequency  $\omega/|\omega_{*e}|$  of TEMs as a function of the collisionality for both the pure and carbon RFP plasmas. Comparing the growth rates in Figs. 9(a) and 9(c), we find that when there are impurities, the growth rates for both the hollow and non-hollow density distributions are significantly lower than those obtained in the cases without impurities. At the same time, for a hollow density profile, the growth rate of the TEMs is considerably less affected by impurity ions. On the other hand, due to the impact of

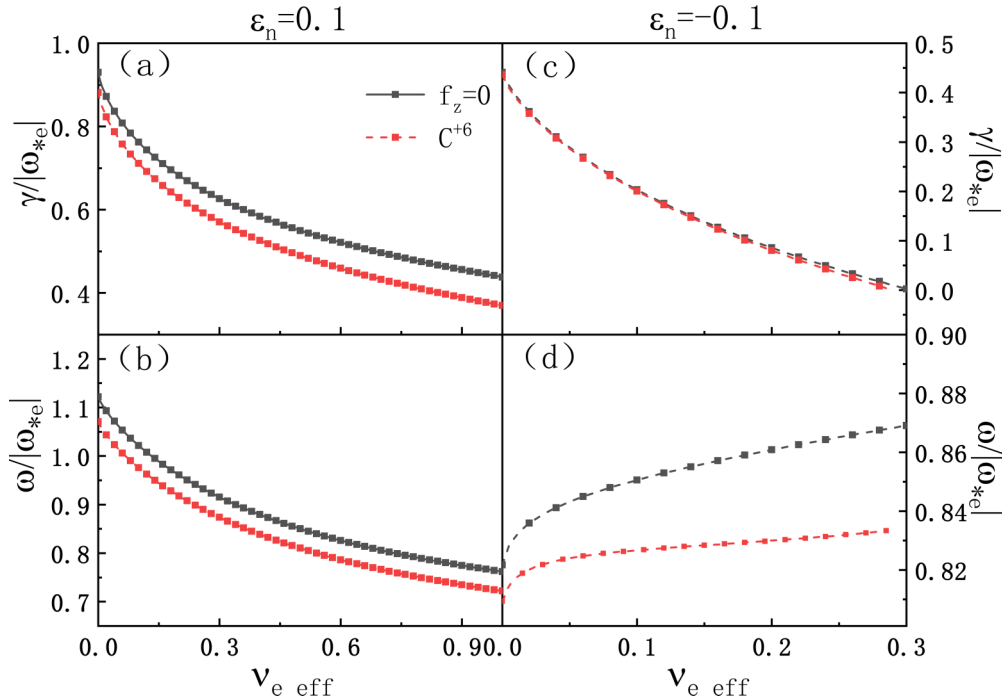


FIG. 9. Real frequency  $\omega/|\omega_{*e}|$  and growth rate  $\gamma/|\omega_{*e}|$  versus collisionality for pure plasma ( $f_z = 0$ ) and plasma in presence of carbon impurity ( $f_z = 0.1$  and  $L_{ez} = 2$ ). The other parameters are the same as those used in Fig. 6.

the collision rate, the TEM growth rate will decrease. This is because the trapped electrons can collide without completing a “banana” orbit, and the collision affects the TEM driving source. Therefore, the TEMs are damped by the collisionality.

Our results show that the instability interval of the TEM mode in RFP plasmas is much smaller than that of tokamak plasmas. For example, when the plasma density gradient is small, a high electron temperature gradient is required to excite the TEMs. The main reason for this is that there is a higher ion Landau damping in RFP plasmas than in tokamak plasmas (the lower  $q$  in RFPs will result in a more significant Landau damping [29]). Our simulations show that the Landau damping cannot only suppress the ITG mode; that is, as the Landau damping increases, the free energy that drives the ITG mode is reduced, and the ITG mode becomes more stable. Indeed, the Landau damping can also stabilize the TEMs. We found that when the effective ion Landau damping frequency changes with respect to the electron precession resonance by increasing the temperature ratio  $\tau$ , that is, reducing the ion Landau damping, the growth rate of the TEMs and the TEM stable interval increase. Therefore, the high Landau damping in RFP plasmas makes it difficult to excite the TEMs.

Interestingly, a reversed density profile can further stabilize the TEMs in RFP plasmas but cannot eliminate the TEMs. A possible reason is that the precession drift of the trapped electrons does not depend on the density gradient. The rotation direction of the TEMs for the hollow density profile case is changed, making the resonance effect of the trapped electrons and modes invalid. Hence, the TEM instability becomes very weak (the collisionless TEM excitation is mainly due to the resonance of the instabilities and the precession drift of the trapped electrons). These results are qualitatively consistent with those of Tang *et al.* [37].

### III. SUMMARY

The gyrokinetic theory was used to study the impact of impurities on the drift wave instability in toroidal plasmas with regular and hollow density profiles. Both collisionless and collisional RFP plasmas with normal and hollow density profiles were considered.

The first part of the article discussed the ITG investigations. For situations with impurities, we found that when  $L_{ez}$  is positive, impurities can reduce the ITG instability, while they can increase the instability when  $L_{ez}$  is negative; the greater the concentration of impurities, the more pronounced this phenomenon.

The main new and novel content of the part of ITG lies in the ITG instability investigation under RFP hollow plasma density. These results have never been achieved before, and the influence of impurities such as tungsten has also been added and clarified. The new outcomes included, by comparing the results of the regular ( $\epsilon_n > 0$ ) and hollow ( $\epsilon_n < 0$ ) plasma density profiles, it is shown that the growth rate of the former is smaller, the instability interval is smaller, and the ITG instability is harder to excite. The influence of  $L_{ez}$  on the ITG instability for plasmas with hollow and non-hollow density profiles is the same. The growth rate of the ITG mode gradually decreases with the increase in the impurity mass.

That is, heavy impurities, such as tungsten, have a better stabilizing effect on the ITG mode.

In the second part, the present work focused on studying the influence of different impurities on the TEM instability. The selected impurities were fully ionized carbon, oxygen, and tungsten. Through simulations, we found that the TEM growth rate for the hollow density case is still lower than that for the normal density case. Moreover, for the concave density profile, the change in the TEMs and  $L_{ez}$  is similar to that of the ITG mode with  $L_{ez}$  with impurities. That is, as  $L_{ez}$  increases (from negative to positive), the growth rate of the TEMs decreases. There is a threshold value for  $L_{ez}$ . When  $L_{ez}$  is less than this threshold, the impurities destabilize the TEMs, while when  $L_{ez}$  is greater than this threshold, the impurities stabilize the TEMs. The results are the opposite in the case of W impurities. Tungsten is unique due to its high mass number. The TEMs are harder to excite when W impurities are incorporated, suggesting that W is an ideal first-wall material.

Finally, the impact of collisionality on the TEM instability was studied. The simulation results show that, considering the collisionality, the growth rate of the TEMs decreases with increasing the collision rate, which is consistent with previous calculation results. We have clarified the physics underlying the TEMs. Besides, the instability threshold analysis in this article will provide a reference for comparing simulation and experimental results.

Work involving electromagnetic simulations of the ITG and TEMs in toroidal plasmas is ongoing alongside comparisons of the drift wave characteristics in both RFP and tokamak plasmas.

### ACKNOWLEDGMENTS

This work is supported by the National Natural Science Foundation of China (Grants No. 11905109, No. 11905080, No. 12275354, and No.11947238), the National Key R&D Program of China (Grants No. 2018YFE0303102 and No. 2017YFE0301702), and the Center for Computational Science and Engineering of Southern University of Science and Technology.

### APPENDIX: THE DERIVATION OF THE TE DENSITY RESPONSE IN RFP

The gyrokinetic equation satisfied by the electrons in RFP reads

$$\left[ i \frac{\hat{v}_{\parallel} v_{te}}{Rq\alpha} \frac{\partial}{\partial \eta} + (\omega - \omega_{d,e}) \right] \delta H_{e0} = -(\omega - \omega_{*Te}) F_{Me} \frac{e\delta\phi}{T_e}. \quad (\text{A1})$$

The parameters in the equation are

$$\omega_{d,e} = -k_{\theta}(2T_e c/eB)[(\hat{v}_{\perp}^2/2)/L_B + (\epsilon^2/q^2\alpha^2)\hat{v}_{\parallel}^2/r],$$

$$k_{\theta} = \frac{nq}{r}\alpha, \alpha = \sqrt{1 + \epsilon^2/q^2},$$

$$L_B = -\left(\frac{d \ln B}{dr}\right)^{-1},$$

$$\omega_{*Te} = \omega_{*e}[1 + \eta_e(\hat{v}_{\perp}^2 + \hat{v}_{\parallel}^2 - 3/2)],$$

$$\eta_e = \frac{L_n}{L_T},$$

$$F_{Me} = \frac{n_e}{\pi^{\frac{3}{2}} v_{te}^3} \exp(-\hat{v}_\perp^2 - \hat{v}_\parallel^2),$$

where  $v_{te}$  is the thermal velocity of electrons,  $\delta\phi$  is the disturbed electrostatic potential.  $n_e$  is electron density.  $T_e$  is the temperature of electrons.

For TEMs, there exists an order of magnitude relationship:

$$\omega_{b,i} \ll \omega_{d,i}, \omega_{t,i}, \langle \omega_{d,e} \rangle \leq \omega \ll \omega_{b,e} \ll \omega_{t,e},$$

where  $\omega_{b,i}$ ,  $\omega_{b,e}$  are the bouncing frequency  $\omega_{t,i}$ ,  $\omega_{t,e}$  the transit frequency  $\omega_{d,i}$ ,  $\omega_{d,e}$  the diamagnetic drift frequency.  $\langle \rangle$  is the bounce average.

The non-adiabatic perturbation distribution function can be written as

$$\delta H_{e0} = \delta H_{e0}^{(0)} + \delta H_{e0}^{(1)}. \quad (\text{A2})$$

According to  $\langle \omega_{d,e} \rangle \leq \omega \ll \omega_{b,e}$  and  $\omega_{b,e} = \frac{1}{\tau_{b,e}} = \frac{1}{2 \int_{-\theta_0}^{\theta_0} \frac{qR_0}{|v_\parallel|} d\theta}$  then the lowest order form of the equation is

$$\frac{\partial \delta H_{e0}^{(0)}}{\partial \eta} = 0. \quad (\text{A3})$$

Namely, under the above frequency conditions, the lowest-order perturbation distribution function does not change along the magnetic field lines. Expanding the gyrokinetic equation to the first order, one can get

$$\left[ i \frac{2\hat{v}_\parallel v_{te}}{Rq\alpha} \frac{\partial \delta H_{e0}^{(1)}}{\partial \eta} + (\omega - \omega_{d,e}) \delta H_{e0}^{(0)} \right] = -(\omega - \omega_{*Te}) F_{Me} \frac{e\delta\phi}{T_e}. \quad (\text{A4})$$

Since  $\delta H_{e0} = \delta H_{e0}^{(0)} + \delta H_{e0}^{(1)}$ , and  $\delta H_{e0}$  satisfies the poloidal periodicity, so as  $\delta H_{e0}^{(1)}$  satisfies the poloidal periodicity, then the first term after the bounce average is 0. The equation then becomes

$$(\omega - \langle \omega_{d,e} \rangle) \delta H_{e0}^{(0)} = -(\omega - \omega_{*T}) F_{Me} \frac{e\langle \delta\phi \rangle}{T_e} \quad (\text{A5})$$

and we have

$$\begin{aligned} \langle \omega_{d,e} \rangle &= \frac{\int_{-\theta_0}^{\theta_0} \frac{\omega_{d,e}}{|v_\parallel|} d\theta}{\int_{-\theta_0}^{\theta_0} \frac{d\theta}{|v_\parallel|}} \\ &= \frac{\frac{\omega_{deB}}{2} \int_{-\theta_0}^{\theta_0} \frac{\hat{v}_\perp^2}{|v_\parallel|} d\theta + \omega_{deC} \int_{-\theta_0}^{\theta_0} \frac{\hat{v}_\parallel^2}{|v_\parallel|} d\theta}{\int_{-\theta_0}^{\theta_0} \frac{d\theta}{|v_\parallel|}} \\ &= - \left\{ \omega_{deB} t \frac{1}{2} \left\{ 1 + 2\xi \left[ 1 - \kappa^2 - \frac{E(\kappa)}{K(\kappa)} \right] \right\} \right. \\ &\quad \left. + \omega_{deC} t \frac{1}{2} \left[ 4\xi (\kappa^2 - 1 + \frac{E(\kappa)}{K(\kappa)}) \right] \right\}. \end{aligned}$$

Here,  $\omega_{d,e}$  includes the magnetic gradient drift frequency  $\omega_{deB} (= \omega_{*e} L_n / L_B)$  and the magnetic curvature drift frequency  $\omega_{deC} (= k_\theta (T_e c / eB) \epsilon^2 / q^2 \alpha^2 r)$ .  $\xi = \epsilon B_{\phi 0}^2 + \zeta B_{\theta 0}^2$ ,  $\zeta = k_\perp^2 v_{te}^2 / \Omega^2$ ,  $\Omega = eB / mc$ ,  $k_\perp$  is the wave number in the direction perpendicular to magnetic field.  $K(\kappa)$  and  $E(\kappa)$  are the complete elliptic integrals of the first and second kinds, respectively, and  $t = v^2 / v_{te}^2$ ,  $\theta_r$  is the returning point in banana orbit for trapped electrons, corresponding to the case where the parallel velocity of electron is zero.

At the same time, it should be noted that the inflection point  $X$  corresponds to the coordinates of the magnetic field line. Then, in the space of ballooning mode, due to the existence of the inflection point, the trapped electrons are confined in many sub-intervals along the direction of the magnetic field, which can be expressed by the  $\delta$  function

$$\begin{aligned} \langle \delta\phi \rangle &= \frac{1}{4K(\kappa)} \int_{-\theta_0}^{\theta_0} \frac{\delta\phi d\theta}{\sqrt{\kappa^2 - \sin^2 \frac{\theta}{2}}} \\ &= \sum_{j=-\infty}^{\infty} \left[ \int_{2\pi j - \pi}^{2\pi j + \pi} \delta(\theta - \theta') d\theta' \int_{2\pi j - \theta_0}^{2\pi j + \theta_0} \frac{\delta\phi d\theta}{4K(\kappa) \sqrt{\kappa^2 - \sin^2 \frac{\theta}{2}}} \right], \end{aligned}$$

where  $\delta(x)$  is Dirac's  $\delta$  function. So the final result of the bounce average is

$$\delta H_{e0}^{(0)} = - \frac{\omega - \omega_{*Te}}{\omega - \langle \omega_{d,e} \rangle} \frac{eF_{Me}}{T_e} \times \sum_{j=-\infty}^{\infty} \left[ \int_{2\pi j - \pi}^{2\pi j + \pi} \delta(\theta - \theta') d\theta' \int_{2\pi j - \theta_0}^{2\pi j + \theta_0} \frac{\delta\phi d\theta}{4K(\kappa) \sqrt{\kappa^2 - \sin^2 \frac{\theta}{2}}} \right]. \quad (\text{A6})$$

Integrating the guiding centered non-adiabatic perturbation distribution function of trapped electrons in the velocity space, we can get

$$\begin{aligned} \iiint \delta H_{e0}^{(0)}(\kappa^2, v^2) d^3v &= - \frac{en_{e0}}{T_e} \sqrt{\frac{2\xi}{\pi}} \int_0^\infty \frac{\omega - \omega_{*Te}}{\omega - \langle \omega_{d,e} \rangle} e^{-\hat{v}^2} \hat{v} d\hat{v}^2 \int_{\sin^2 \frac{\theta}{2}}^1 \frac{d\kappa^2}{\sqrt{\kappa^2 - \sin^2 \frac{\theta}{2}}} \\ &\quad \times \sum_{j=-\infty}^{\infty} \left[ \int_{2\pi j - \pi}^{2\pi j + \pi} \delta(\theta - \theta') d\theta' \int_{2\pi j - \theta_0}^{2\pi j + \theta_0} \frac{\delta\phi(\theta) d\theta}{4K(\kappa) \sqrt{\kappa^2 - \sin^2 \frac{\theta}{2}}} \right]. \quad (\text{A7}) \end{aligned}$$

Changing the order of integration, and introducing

$$g(\eta, \kappa) = \int_{-\theta_r}^{+\theta_r} \frac{\delta(\eta - \theta') d\theta'}{\sqrt{\kappa^2 - \sin^2 \frac{\theta'}{2}}}.$$

Equation (A7) then can be simplified to

$$\tilde{n}_{te} = -\frac{en_{0e}}{T_e} \sqrt{\frac{2\xi}{\pi}} \int_0^{+\infty} dt \sqrt{t} e^{-t} \frac{\omega - \omega_{*Te}}{\omega - \langle \omega_{d,e} \rangle} \times \int_0^1 \frac{d\kappa^2}{4K(\kappa)} \sum_{j=-\infty}^{+\infty} g(\theta - 2\pi j, \kappa) \times \int_{-\infty}^{+\infty} d\theta' g(\theta', \kappa) \phi(\theta' - 2\pi j). \quad (\text{A8})$$

So far we have derived the term of the TE density response. It should be noted that in comparison with Ref. [30], we ignore the collisionality here, whose effect can be added in Eq. (A8) directly.

- 
- [1] W. Horton, *Rev. Mod. Phys.* **71**, 735 (1999).  
 [2] F. Wagner *et al.*, *Phys. Rev. Lett.* **49**, 1408 (1982).  
 [3] H. Zhu, Y. Zhou, D. E. Ruiz, and I. Y. Dodin, *Phys. Rev. E* **97**, 053210 (2018).  
 [4] R. A. Heinonen and P. H. Diamond, *Phys. Rev. E* **101**, 061201(R) (2020).  
 [5] X. Garbet, *Plasma Phys. Control. Fusion* **43**, A251 (2001).  
 [6] Z. Lin *et al.*, *Science* **281**, 1835 (1998).  
 [7] A. Hasegawa, *Phys. Fluids* **12**, 2642 (1969).  
 [8] J. Li *et al.*, *Plasma Phys. Control. Fusion* **63**, 125005 (2021).  
 [9] F. Romanelli, *Phys. Fluids B* **1**, 1018 (1989).  
 [10] F. Sattin *et al.*, *J. Phys.: Conf. Ser.* **260**, 012018 (2010).  
 [11] J. R. Duff *et al.*, *Phys. Plasmas* **25**, 010701 (2018).  
 [12] Z. R. Williams *et al.*, *Phys. Plasmas* **24**, 122309 (2017).  
 [13] C. Angioni *et al.*, *Nucl. Fusion* **57**, 116053 (2017).  
 [14] M. Valovič *et al.*, *Nucl. Fusion* **48**, 075006 (2008).  
 [15] G. A. Wurden *et al.*, *Nucl. Fusion* **27**, 857 (1987).  
 [16] B. Baiocchi *et al.*, *Nucl. Fusion* **55**, 123001 (2015).  
 [17] M. Zuin *et al.*, *Nucl. Fusion* **57**, 102012 (2017).  
 [18] T. Barbui *et al.*, *Plasma Phys. Control. Fusion* **57**, 025006 (2015).  
 [19] B. Pégourié, *Plasma Phys. Control. Fusion* **49**, R87 (2007).  
 [20] D. Xuan-Tong *et al.*, *Chin. Phys. Lett.* **23**, 2502 (2006).  
 [21] R. Lorenzini *et al.*, *Plasma Phys. Control. Fusion* **44**, 233 (2002).  
 [22] M. D. Wyman *et al.*, *Nucl. Fusion* **49**, 015003 (2009).  
 [23] R. Sakamoto *et al.*, *Nucl. Fusion* **46**, 884 (2006).  
 [24] L. Garzotti *et al.*, *Plasma Phys. Controlled Fusion* **56**, 035004 (2014).  
 [25] J. Q. Dong *et al.*, *Phys. Plasmas* **8**, 3635 (2001).  
 [26] J. Li *et al.*, *Plasma Sci. Technol.* **22**, 055101 (2020).  
 [27] I. Predebon *et al.*, *Plasma Phys. Control. Fusion* **53**, 125009 (2011).  
 [28] J. C. Li *et al.*, *Europhys. Lett.* **127**, 45002 (2019).  
 [29] S. C. Guo, *Phys. Plasmas* **15**, 122510 (2008).  
 [30] S. F. Liu *et al.*, *Nucl. Fusion* **54**, 043006 (2014).  
 [31] S. F. Liu *et al.*, *Nucl. Fusion* **51**, 083021 (2011).  
 [32] L. Marrelli *et al.*, *Nucl. Fusion* **61**, 023001 (2021).  
 [33] Y. Yao *et al.*, *Nucl. Fusion* **62**, 086031 (2022).  
 [34] I. Predebon *et al.*, *Phys. Plasmas* **17**, 012304 (2010).  
 [35] F. Sattin *et al.*, *Plasma Phys. Control. Fusion* **52**, 105002 (2010).  
 [36] F. Jenko *et al.*, *Phys. Plasmas* **7**, 1904 (2000).  
 [37] W. M. Tang *et al.*, *Phys. Rev. Lett.* **35**, 660 (1975).